EDGE ARTICLE

Check for updates

A bottom-up synthesis of rare-earth-hydrotalcite monolayer nanosheets toward multimode imaging and synergetic therapy†

Xuan Mei, Jialing Ma, Xue Bai, Xin Zhang, Shaomin Zhang, Ruizheng Liang,* Min Wei, [ID] * David G. Evans and Xue Duan

Recently, ultrathin two-dimensional (2D) nanomaterials have attracted considerable research interest in biomedical applications, owing to their intriguing quantum size and surface effects. In this work, a one-step "bottom-up" method is developed to prepare rare-earth (Gd^{3+} and Yb^{3+}) co-doped layered double hydroxide (LDH) monolayer nanosheets, with a precisely controlled composition and uniform morphology. Due to the successful introduction of Gd^{3+} and Yb^{3+} into the LDH host layer, the Gd&Yb-LDH monolayer nanosheets exhibit excellent magnetic resonance (MR)/X-ray computed tomography (CT) dual-mode imaging functionality. Moreover, the Gd&Yb-LDH monolayer nanosheets achieve an ultrahigh loading of a chemotherapeutic drug (SN38) with a loading content (LC) of 925%, which is a one order of magnitude enhancement compared with previously reported delivery systems of hydrophobic drugs. Interestingly, by further combination with indocyanine green (ICG), *in vivo* tri-mode imaging, including CT, MR and near infrared fluorescence (NIRF) imaging, is achieved, which enables a noninvasive visualization of cancer cell distribution with deep spatial resolution and high sensitivity. In addition, *in vitro* and *in vivo* therapeutic evaluations demonstrate an extremely high tri-mode synergetic anticancer activity and superior biocompatibility of SN38&ICG/Gd&Yb-LDH. Therefore, this work demonstrates a paradigm for the synthesis of novel multifunctional 2D monolayer materials *via* a facile "bottom-up" route, which shows promising applications in cancer synergetic theranostics.

Introduction

Recently, increasingly interdisciplinary research efforts have been devoted to exploring biomedical applications of ultrathin two-dimensional (2D) nanomaterials such as graphene,[1] black phosphorus (BP),[2] hexagonal boron nitride (h-BN)[3] and transition-metal dichalcogenides (TMDs),[4] due to their extraordinary quantum size and surface effects.[5] Their intrinsic physicochemical and electronic properties make them promising candidates for a variety of imaging techniques (*e.g.* magnetic resonance (MR), X-ray computed tomography (CT), and photoacoustics (PA)) and photothermal therapy.[6] Although much progress has been made,[7] the most studied ultrathin 2D nanomaterials, normally synthesized by exfoliation of bulk precursors, suffer from fixed chemical composition with uncontrollable functionality. The lack of universal and gentle methods to prepare ultrathin or monolayer 2D nanomaterials is still the key scientific problem in 2D nanomaterials.[8] Therefore, if monolayer 2D nanomaterials with a fine control over morphology, thickness, chemical composition and functionality can be prepared by a universal bottom-up chemical synthesis method, the intrinsic performance of 2D nanomaterials would be observably promoted.

Layered double hydroxides (LDHs), a typical 2D nanomaterial with the formula $[M_{1-x}^{2+}M_x^{3+}(OH)_2](A^{n-})_{x/n} \cdot mH_2O$, are made up of positively charged, edge-sharing MO_6 octahedral host layers and exchangeable interlayer anions.[9] Due to the unique 2D structure with tunability in both host layer and interlayer anions, LDHs have shown potential for application as drug carriers in biomedicine.[10] For example, LDHs have been demonstrated as an efficient drug formulation for delivery and controlled release of drug molecules owing to their low toxicity and good biocompatibility.[11,12] Although a synthetic strategy for LDHs has been developed,[13] the preparation of LDH monolayer nanosheets with precise control over chemical compositions and regulation of monolayer functionality is still an obstacle and hasn't been resolved yet. Moreover, hydrophobic drugs like SN38 possesses 100–1000 times stronger anticancer performance than their modified hydrophilic drugs (camptothecin-11);[14] however, their application is greatly limited by their poor water solubility, and the current drug carriers usually exhibit

State Key Laboratory of Chemical Resource Engineering, Beijing Advanced Innovation Center for Soft Matter Science and Engineering, Beijing University of Chemical Technology, Beijing 100029, P. R. China. E-mail: liangruizheng2000@163.com; weimin@mail.buct.edu.cn

poor loading content (LC). Enhancing the loading and controlled release of hydrophobic drugs like SN38 is highly needed but remains a big challenge.

Herein, we designed and prepared Gd^{3+} and Yb^{3+} co-doped LDH monolayer nanosheets *via* a one-step "bottom-up" method, which exhibited excellent dual-model imaging functionality. HRTEM and AFM show that Gd&Yb-LDH nanosheets possess a uniform lateral size of ∼50 nm and a thickness of ∼0.9 nm, corresponding to a single sheet of LDH matrix. EDX and XPS spectroscopy verify the successful co-doping of Gd^{3+} and Yb^{3+} into the LDH host layer. Moreover, Gd&Yb-LDH monolayer nanosheets achieve an ultrahigh loading of chemotherapeutic drug SN38 with a LC of 925%, which is a one order of magnitude enhancement compared with previously reported delivery systems of hydrophobic drugs.[14] The as-prepared SN38&ICG/Gd&Yb-LDH shows a controlled drug release behavior with pH stimuli or NIR irradiation, as well as significantly enhanced photothermal and photodynamic performance. *In vitro* tests verify a superior anticancer efficacy of SN38&ICG/Gd&Yb-LDH with an IC_{50} value of 0.532 µg mL^{-1}, significantly lower than that of pristine SN38 (5.80 µg mL^{-1}) or ICG (1.89 µg mL^{-1}). *In vivo* MR/CT/near infrared fluorescence (NIRF) tri-mode imaging exhibits an excellent passive targeted tumor accumulation of SN38&ICG/Gd&Yb-LDH, and a complete tumor ablation is realized after treatment with SN38&ICG/Gd&Yb-LDH, demonstrating a promising synergetic theranostics performance.

Results and discussion

Structural characterization

To realize MR and CT imaging, a new "bottom-up" method is developed to synthesize Gd&Yb-containing LDH monolayer nanosheets (see the Experimental section for details), where Gd^{3+} and Yb^{3+} are simultaneously introduced into an LDH matrix (molar content: 10% each). As shown in Fig. S1,† ultrathin Gd&Yb-LDH nanosheets are prepared through a bottom-up hydrothermal synthesis with a yield of 15.4%. Fig. 1A shows the high resolution transmission electron microscopy (HRTEM) image of monodisperse, hexagonal Gd&Yb-LDH nanosheets with a lateral size of ∼50 nm, and the lattice fringe of 0.178 nm in the inset can be ascribed to the LDH [110] plane. The dynamic light scattering technique gives an equivalent hydrodynamic diameter of 50 ± 9.5 nm in water, phosphate buffered saline (PBS) or culture medium (Fig. S2†). After storage for two weeks, no obvious change in the hydrodynamic size of Gd&Yb-LDH was found (Fig. S3†), demonstrating its long-term stability. The elemental distributions obtained from energy-dispersive X-ray (EDX) mapping (Fig. 1B) and the corresponding EDX line profile (Fig. S4†) reveal that Mg, Al, Gd and Yb are homogeneously distributed throughout the LDH nanosheets, indicating the co-doping of Gd and Yb into the LDH matrix. This is further confirmed by X-ray photoelectron spectroscopy (XPS) peaks at 1185.2 eV and 185.4 eV, corresponding to the characteristic peaks of Gd 3d and Yb 4d, respectively (Fig. 1C and D). Atomic force microscopy (AFM) images verify that the Gd&Yb-LDH nanosheets possess a monolayer thickness of ∼0.9 nm (Fig. 1E

and F), close to that obtained using the liquid delamination method.[15] The monolayer structure of Gd&Yb-LDH nanosheets is further confirmed by X-ray diffraction (XRD) analysis. The Gd&Yb-LDH colloid sample doesn't show the characteristic reflection of the LDH phase (Fig. 1G; green line), in contrast to the (003) peak at $2\theta = 10.22°$ for an LDH bulk sample (Fig. 1G; blue line), indicating the absence of the multilayer structure. However, after drying the Gd&Yb-LDH colloid sample, a (003) reflection at 10.28° is observed, which is due to the re-stacking of the LDH monolayer to the bulk material (Fig. 1G; red line). Taking into account MRI and CT dual-mode contrast agents, the relevant parameters of Gd&Yb-LDH were evaluated. The T_1-weighted relaxivity (r_1, a key parameter in MRI) value of Gd&Yb-LDH is determined to be 9.00 mM^{-1} s^{-1} (Fig. 1H), while the CT value shows a positive enhancement against concentration with a slope of 66.3 (Fig. 1I), which are 2.47 and 2.20 fold respectively larger than that of commercial MRI (Gd-DOTA)[16] and CT (iobitridol) contrast agents.[17]

Drug loading performance

The loading performance of Gd&Yb-LDH nanosheets toward ICG and SN38 was studied. For separate loading of ICG, the loading content (LC) and encapsulation efficiency (EE) are 196% and 98.1% with a nominal mass ratio of drug : LDH = 2 : 1 (Fig. 2A). The LC increases slightly but the EE decreases obviously along with the increase of ICG : Gd&Yb-LDH mass ratio. For the loading of SN38, the LC and EE are 794% and 99.3% with a mass ratio of drug : LDH = 8 : 1 (Fig. 2B), giving an ultrahigh LC value at close to 100% EE. Most importantly, the LC of SN38 reaches 925% with a mass ratio of SN38 : Gd&Yb-LDH = 10 : 1, which is a one order of magnitude enhancement compared with previously reported delivery systems of hydrophobic drugs (Table S1†).[14] Subsequently, we further investigated the co-loading of SN38 and ICG (mass ratio of 2 : 1) onto the Gd&Yb-LDH nanosheets. The largest co-loading LC is found to be 1105% (SN38 : ICG : Gd&Yb-LDH = 10 : 5 : 1); however, taking into account both LC and EE, the final mass ratio is determined to be SN38 : ICG : Gd&Yb-LDH = 4 : 2 : 1, for which the LC and EE values are 595% and 99.1%, respectively (Fig. 2C). The time-dependent adsorption behavior (Fig. 2D) shows a very fast adsorption within the first 5 min and a gentle increment up to 60 min. As shown in the Fourier transform infrared (FT-IR) spectra (Fig. 2E), bands at 1735 cm^{-1} (stretching vibration of C=O) for SN38 and 1423 cm^{-1} (stretching vibration of C=C) for ICG are observed in the final sample, accompanied by the characteristic band of LDH at 445 cm^{-1} (vibration absorption peak of O–M–O), indicating the co-loading of SN38 and ICG onto LDH nanosheets. The combination is further confirmed in the UV-vis-NIR spectra (Fig. 2F), where SN38&ICG/Gd&Yb-LDH exhibits both the absorption peaks of SN38 and ICG. Moreover, due to the monodisperse state of ICG on Gd&Yb-LDH nanosheets, SN38&ICG/Gd&Yb-LDH shows a 1.21-fold absorption enhancement compared to pristine ICG, which is beneficial to the photothermal conversion. In addition, the zeta potential of SN38&ICG/Gd&Yb-LDH is measured to be −14.5 mV (Fig. 2G), which is ascribed to the immobilization of negatively charged
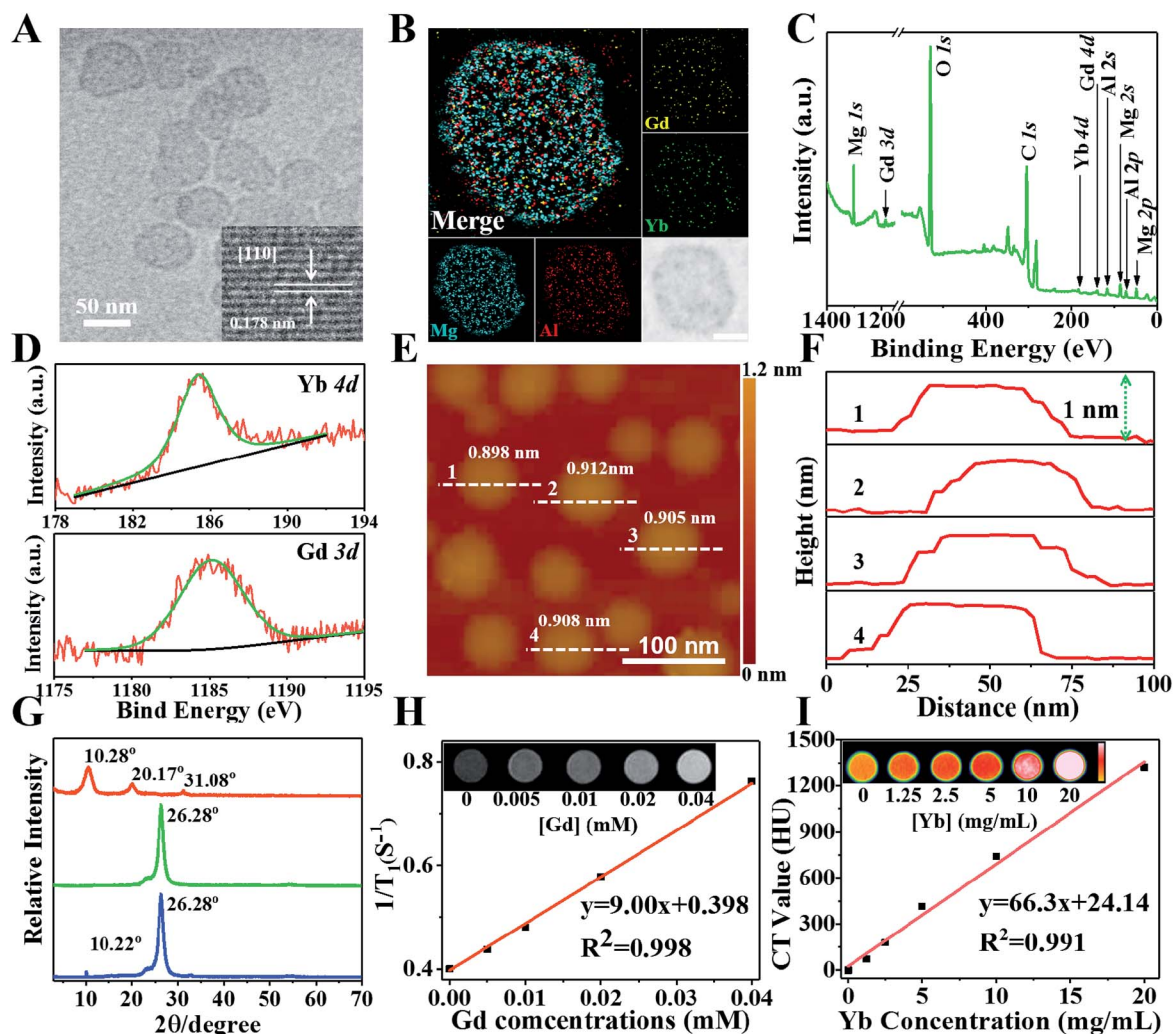
Fig. 1 (A) HRTEM image of monolayer Gd&Yb-LDH. The inset shows the [110] lattice fringe of an LDH phase. (B) EDX mapping of Gd&Yb-LDH monolayer nanosheets. Scale bar, 20 nm. (C) Wide XPS spectra of Gd&Yb-LDH nanosheets and (D) XPS spectra of Gd 3d and Yb 4d. (E) AFM image and (F) measured thickness of the Gd&Yb-LDH monolayer nanosheets. (G) XRD patterns of the bulk LDH sample (blue), the Gd&Yb-LDH monolayer sample (green), and the re-stacked sample of Gd&Yb-LDH monolayers (red). The peak at 26.28° is ascribed to the PET substrate. (H) T_1-Weighted relaxivity and MRI images (inset) of the Gd&Yb-LDH monolayer with various Gd concentrations. (I) CT value and CT images (inset) of the Gd&Yb-LDH monolayer with various Yb concentrations.

SN38&ICG (−21.1 mV) onto positively charged Gd&Yb-LDH nanosheets (+38.0 mV).

The HRTEM image (Fig. S5†) shows that the uniform morphology of SN38&ICG/Gd&Yb-LDH is well maintained after the co-loading of SN38 and ICG, with a diameter of ~60 nm. Moreover, its thickness in aqueous solution, which was studied by molecular dynamics (MD) simulations (Fig. S6†), was determined to be 8.4 nm. Fig. S7† displays rather similar hydrodynamic diameters of SN38&ICG/Gd&Yb-LDH in deionized water, PBS and culture medium. Moreover, both Gd&Yb-LDH and SN38&ICG/Gd&Yb-LDH display an obvious Tyndall effect for 14 days (Fig. S8†), indicating high aqueous dispersibility and colloidal stability. The interactions of SN38–ICG and drug–LDH were investigated by isothermal titration calorimetry (ITC) measurements. The SN38–ICG system shows positive values of ΔH and ΔS, indicating hydrophobic interaction between SN38

and ICG, while in the case of SN38&ICG/Gd&Yb-LDH, negative values of both ΔH and ΔS are obtained, demonstrating the existence of van der Waals' force, electrostatic interaction or hydrogen bonding between drug and LDH (Fig. 2H and S9†). To further address the interaction mechanism of drug–LDH and the high drug loading performance, molecular dynamics (MD) simulations were employed (see details in Fig. S6†). As shown in Fig. 2I, both SN38 and ICG give obviously smaller diffusion coefficients (with an average binding energy of −31.1 kcal mol⁻¹ for SN38 and −35.9 kcal mol⁻¹ for ICG) on Gd&Yb-LDH than in water (Fig. S10†), which is ascribed to electrostatic interaction between drug molecules and the Gd&Yb-LDH monolayer. Fig. S11A† displays the O···H–O hydrogen bond with a bond length of 2.0–3.0 Å demonstrated by the radial distribution function (Fig. S11B and C†), indicating a strong hydrogen bond interaction between drug molecules and the Gd&Yb-LDH
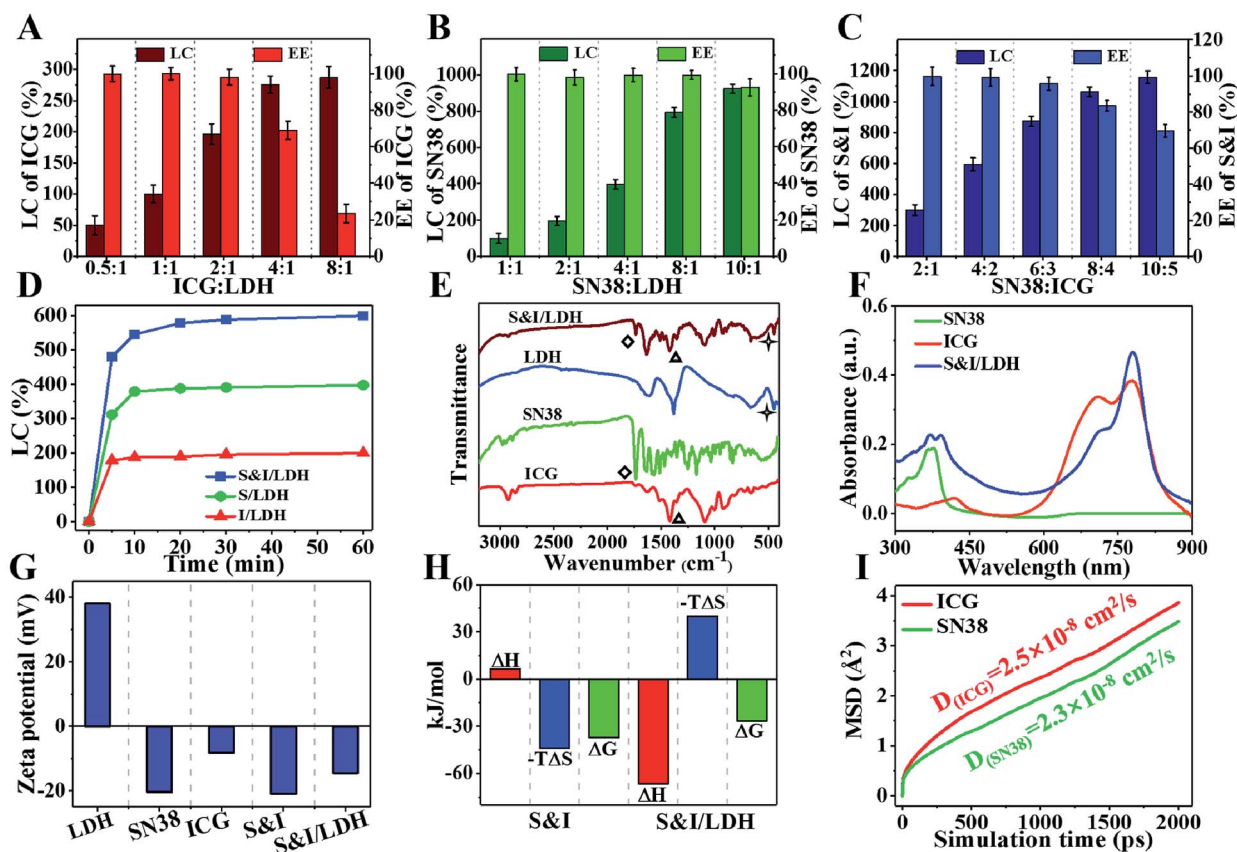
Fig. 2 LC and EE of (A) ICG, (B) SN38 and (C) SN38&ICG onto Gd&Yb-LDH nanosheets with various mass ratios. (D) Time dependent adsorption curves of SN38, ICG and SN38&ICG onto Gd&Yb-LDH nanosheets. (E) FT-IR spectra of pristine ICG, SN38, Gd&Yb-LDH and SN38&ICG/Gd&Yb-LDH, respectively. (F) UV-vis-NIR spectra of SN38, ICG and SN38&ICG/Gd&Yb-LDH. (G) Surface zeta potential of pristine ICG, SN38, Gd&Yb-LDH, SN38&ICG and SN38&ICG/Gd&Yb-LDH. (H) Thermodynamic parameters ΔH, $-T\Delta S$ and ΔG for the SN38–ICG and SN38&ICG-LDH systems, respectively. (I) Mean squared displacement of ICG or SN38 on Gd&Yb-LDH within 2 ns molecular dynamics simulations at 298.15 K.

monolayer. In conclusion, both electrostatic interaction and hydrogen bond play a key role in determining the high drug loading content.

Photothermal study and stimulated drug release

Owing to the intrinsic near-infrared (NIR) optical absorption of ICG, the photothermal conversion performance of SN38&ICG/Gd&Yb-LDH was studied. Fig. 3A shows the temperature elevation in the presence of SN38&ICG/Gd&Yb-LDH, ICG and PBS (concentration of ICG: 2.5 μg mL^{-1}), respectively, upon 808 nm laser irradiation at three power densities (0.5 W cm^{-2}, 1.0 W cm^{-2}, and 1.5 W cm^{-2}). Within 3 min of irradiation, the SN38&ICG/Gd&Yb-LDH suspension displays a much higher temperature increment (8.8 °C, 13.9 °C and 19.8 °C) in comparison with the pristine ICG suspension (5.8 °C, 9.9 °C and 16.5 °C) and PBS (less than 3 °C). The thermal imaging photographs give a visual observation for the temperature change at 1.0 W cm^{-2} (Fig. 3B), illustrating the superior photothermal performance of SN38&ICG/Gd&Yb-LDH. Moreover, SN38&ICG/Gd&Yb-LDH exhibits a more stable photothermal effect than pristine ICG (Fig. 3C): the latter shows a significant loss after four cycles.

The release behavior of SN38 from SN38&ICG/Gd&Yb-LDH was studied through pH control and NIR laser irradiation. Less than 7.4% of SN38 is released at pH 7.4 after 12 h of incubation (Fig. S12†), indicating a high stability of SN38&ICG/Gd&Yb-LDH in a normal physiological environment. However, 17.3% and 21.3% of SN38 is released at pH 6.5 (tumor microenvironment) and pH 5.5 (cancer cell endosome) over 12 h, respectively, showing a pH triggered release behavior. We further investigated the release performance of SN38&ICG/Gd&Yb-LDH upon NIR laser irradiation at different pH values. As shown in Fig. 3D, with NIR irradiation for 3 min (808 nm, 1.0 W cm^{-2}), the released amount reaches 42.0% (at pH = 7.4), 67.9% (at pH = 6.5) and 79.8% (at pH = 5.5) for SN38, which reveals a synergetic drug release behavior under acidic conditions plus NIR irradiation. In comparison, ICG exhibits a limited released amount under the same conditions with NIR irradiation (Fig. S13†), which is ascribed to the stronger binding energy of ICG with Gd&Yb-LDH nanosheets. The temperature induced SN38 release is confirmed in the MD simulations as well (Table S2 and Fig. S14†), from which the diffusion coefficient of SN38/Gd&Yb-LDH increases from 0.5 × 10^{-8} cm^2 s^{-1} to 10.5 × 10^{-8} cm^2 s^{-1} as the temperature increases from 298.15 K to 328.15 K. Moreover, the color of the SN38&ICG/Gd&Yb-LDH suspension
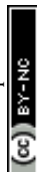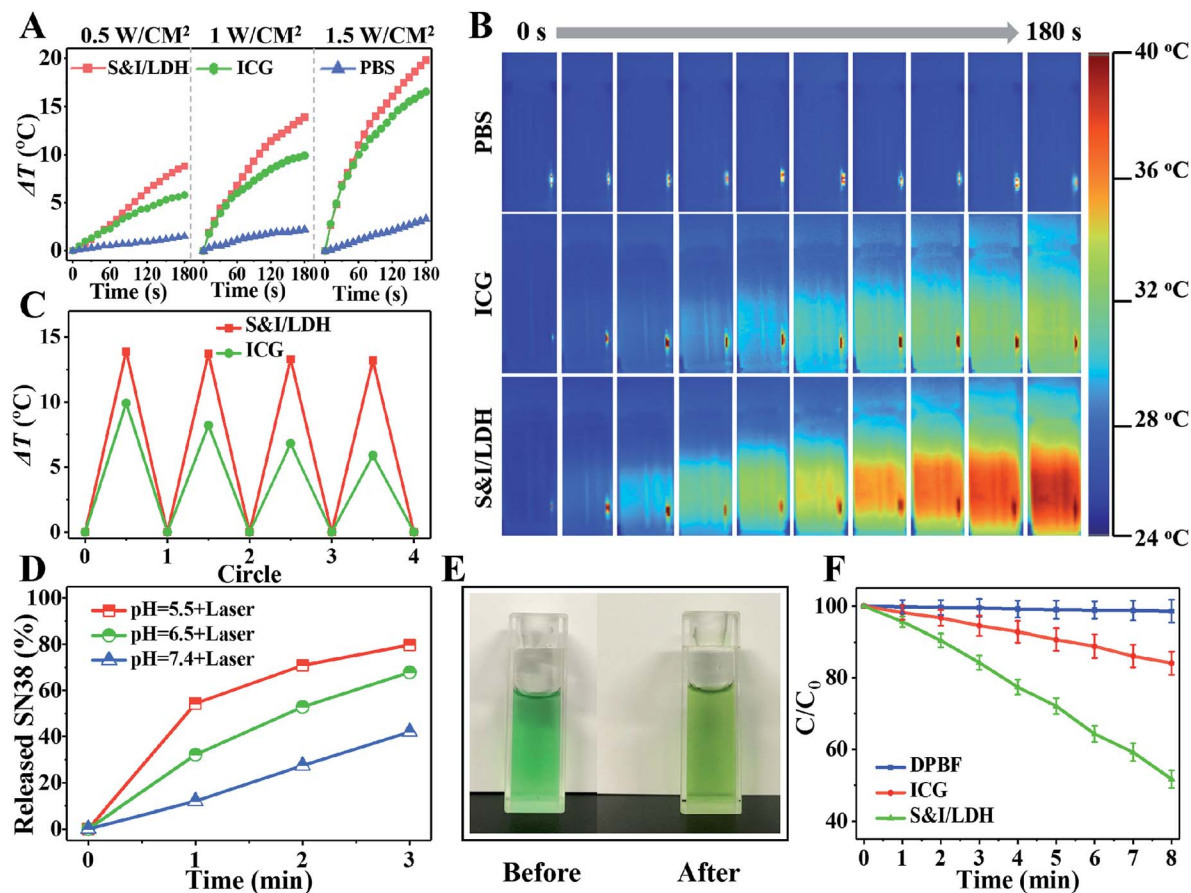
Fig. 3 (A) Photothermal effect of SN38&ICG/Gd&Yb-LDH upon 808 nm irradiation at different power densities (0.5, 1.0, and 1.5 W cm^{-2}), with ICG and PBS as control samples. (B) Photothermal photographs of PBS, ICG and SN38&ICG/Gd&Yb-LDH upon 808 nm irradiation at 1.0 W cm^{-2}. (C) Photostability tests of SN38&ICG/Gd&Yb-LDH and ICG for four cycles. (D) Release curves of SN38 from SN38&ICG/Gd&Yb-LDH in PBS with 808 nm irradiation at pH 5.5, 6.5 and 7.4 (1.0 W cm^{-2}), respectively. (E) Photographs of the SN38&ICG/Gd&Yb-LDH suspension before and after NIR laser irradiation. (F) Normalized absorbance of DPBF in the presence of ICG, SN38&ICG/Gd&Yb-LDH and blank samples with 808 nm irradiation (1.0 W cm^{-2}).

gradually changes from green to yellow (Fig. 3E), accompanied by enhanced fluorescence emission from free SN38 (Fig. S15†), demonstrating a photothermal effect induced SN38 release. In addition, due to the intrinsic photodynamic properties of ICG, the reactive oxygen species (ROS) production of SN38&ICG/Gd&Yb-LDH was measured by using 1,3-diphenylisobenzofuran (DPBF) as a probe[18] (Fig. 3F and S16†). Within 8 min of NIR irradiation, SN38&ICG/Gd&Yb-LDH exhibits a 3.06-fold larger ROS production (proportional to the photodynamic efficiency) than pristine ICG, indicating its better photodynamic performance. The enhanced mono-dispersion of ICG on Gd&Yb-LDH (Fig. 2F) is beneficial to both photothermal conversion and photodynamic therapy, accounting for the increase of ROS production.

In vitro study with Hela cells

To further study the intracellular release behavior, Hela cells were incubated with SN38&ICG/Gd&Yb-LDH for 6 h, and then stained with Hoechst 33342 to mark nuclei.[19] Fig. 4A shows the yellow fluorescence signal of SN38 in the cytoplasm, indicating

the successful endocytosis of SN38&ICG/Gd&Yb-LDH by Hela cells. After 808 nm NIR light irradiation for 3 min, the fluorescence signal is predominantly observed in nuclei, demonstrating an efficient release of SN38 into nuclei from SN38&ICG/Gd&Yb-LDH in the cytoplasm (Fig. 4B). As shown in Fig. S17,† free SN38 exhibits a much stronger fluorescence signal than SN38&ICG/Gd&Yb-LDH with an equal SN38 dose in PBS solution. After irradiation, an efficient release of SN38 is observed from SN38&ICG/Gd&Yb-LDH (in the cytoplasm, Fig. 4A) into nuclei (Fig. 4B), and the fluorescence intensity in nuclei becomes stronger than in the cytoplasm as a result of SN38 release (corresponding to the results in Fig. S17†). This is further confirmed by flow cytometer measurements (Fig. 4C).

In vitro therapeutic performance of SN38&ICG/Gd&Yb-LDH was investigated by a standard methyl thiazolyl tetrazolium (MTT) assay.[20] The cytotoxicity of the Gd&Yb-LDH nanosheets was firstly evaluated by incubation with three kinds of common cancer cells (U87MG, KB and Hela) at concentrations of up to 500 μg mL^{-1} and the MTT results showed little cytotoxicity (Fig. S18†), demonstrating an excellent biocompatibility of Gd&Yb-LDH nanosheets. Subsequently, Hela cells were
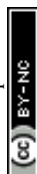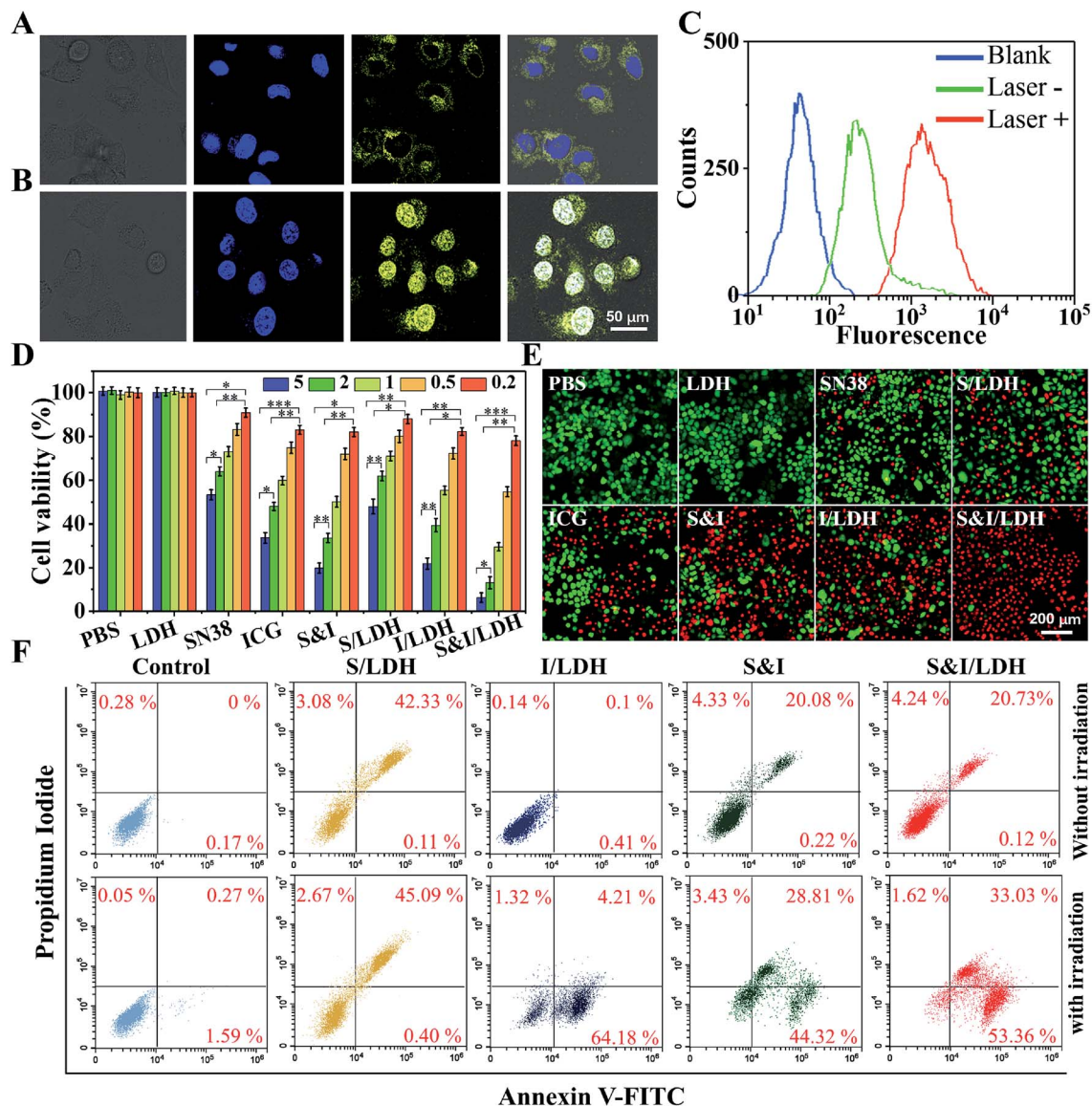
Fig. 4 Confocal images of Hela cells incubated with SN38&ICG/Gd&Yb-LDH: (A) before and (B) after NIR laser irradiation (808 nm, 1.0 W cm^{-2}). (C) Intracellular fluorescence with and without NIR irradiation recorded using a flow cytometer. (D) Viability of Hela cells in the presence of the drugs with different concentrations (from 0.2 to 5.0 μg mL^{-1}) upon NIR irradiation: (1) PBS, (2) Gd&Yb-LDH, (3) SN38, (4) ICG, (5) SN38&ICG, (6) SN38/Gd&Yb-LDH, (7) ICG/Gd&Yb-LDH, and (8) SN38&ICG/Gd&Yb-LDH and (E) the corresponding calcein-AM/PI staining images (5.0 μg mL^{-1}). (F) Cell apoptosis analysis using the PI/annexin V–FITC double staining method. P values in (D) were calculated by Tukey's post-test (***$P < 0.001$, **$P < 0.01$, or *$P < 0.05$).

respectively cultured with PBS, Gd&Yb-LDH, SN38, SN38/Gd&Yb-LDH, ICG, ICG/Gd&Yb-LDH, SN38&ICG and SN38&ICG/Gd&Yb-LDH for 24 h, with the equivalent drug concentration ranging from 0.2 to 5.0 μg mL^{-1}, followed by a thorough washing with PBS. As illustrated in Fig. S19,† MTT results without irradiation show a good biocompatibility in the presence of Gd&Yb-LDH as a drug carrier. After irradiation with 808 nm NIR light (1.0 W cm^{-2}, 3 min), the cellular viability decreases with the drug concentration rising from 0.2 to 5.0 μg mL^{-1} (Fig. 4D). The half maximal inhibitory concentration (IC$_{50}$) values are calculated as below: SN38 (5.80 μg mL^{-1}) > SN38/Gd&Yb-LDH (4.28 μg mL^{-1}) > ICG (1.89 μg mL^{-1}) > ICG/Gd&Yb-LDH (1.25 μg mL^{-1}) > SN38&ICG (1.08 μg mL^{-1}) >

SN38&ICG/Gd&Yb-LDH (0.532 μg mL^{-1}). Based on the IC$_{50}$ value, the combination index (CI, a parameter for evaluation of the synergetic effect of drugs,[21] see the Experimental section for details) of SN38&ICG/Gd&Yb-LDH was calculated to be 0.22 (much lower than 1.0), indicating a significant synergistic effect between SN38 and ICG in this chemo/PTT/PDT tri-mode therapy. To visualize the anticancer efficacy, Hela cells treated with 5 μg mL^{-1} of each of the above samples with irradiation were stained with calcein-AM and propidium iodide (calcein-AM/PI) (Fig. 4E), and SN38&ICG/Gd&Yb-LDH showed the optimal anticancer capability, which is consistent with the results of *in vitro* tests (Fig. 4D). In addition, cell apoptosis was studied using the PI/annexin V–FITC double staining method
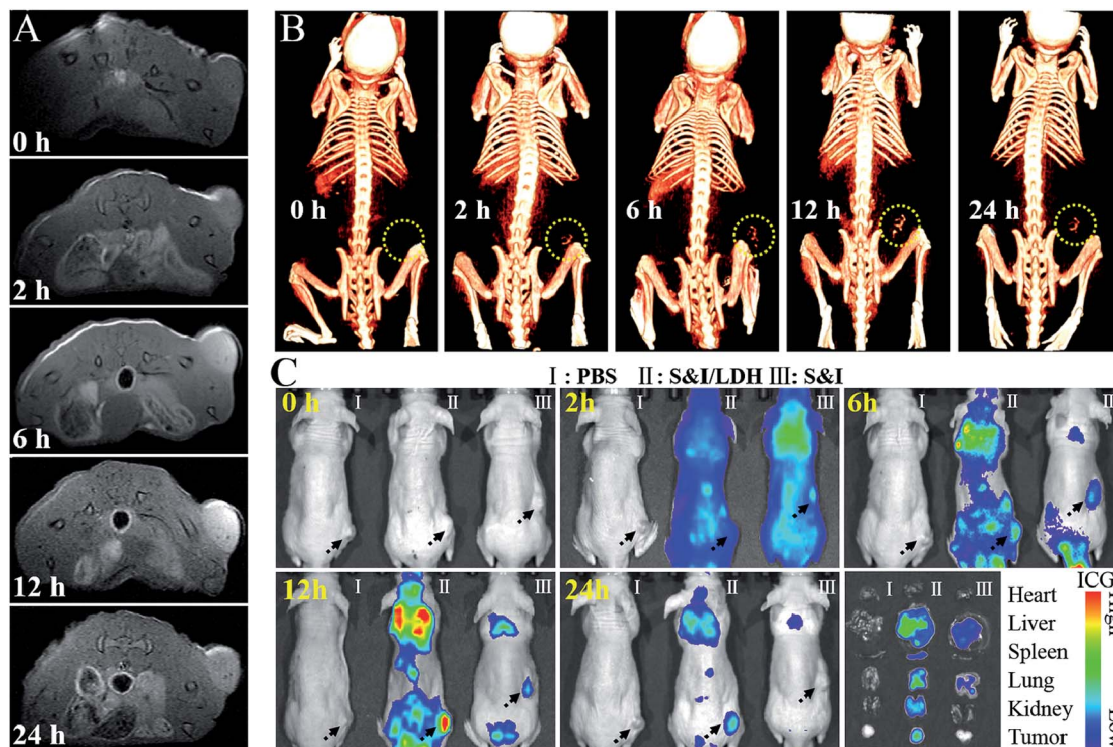
Fig. 5 (A) *In vivo* MR and (B) CT imaging of nude mice bearing Hela tumors at different time points after intravenous injection of SN38&ICG/Gd&Yb-LDH. (C) *In vivo* fluorescence imaging and drug bio-distribution for nude mice bearing Hela tumors at different time points after intravenous injection of PBS, SN38&ICG/Gd&Yb-LDH and SN38&ICG, respectively, together with *ex vivo* imaging of ICG in the tumour and five different organs collected from mice sacrificed at 24 h.

and analyzed by flow cytometry.[22] As shown in Fig. 4F, Hela cells treated with SN38/Gd&Yb-LDH appear in the PI$^+$/annexin V–FITC$^+$ region, indicating a late-stage apoptosis; while an early-stage apoptosis of Hela cells is observed for the sample of ICG/Gd&Yb-LDH. In the case of SN38&ICG/Gd&Yb-LDH, it exhibits both early- and late-stage apoptosis with largely enhanced cell death, demonstrating the combination of chemo/PTT/PDT therapy.

In vivo tri-mode imaging and cancer therapy

All animal procedures were performed in accordance with the National Institute of Health Guiding Principles for the Care and Use of Laboratory Animals and were approved by the Ethics Review Committee for Animal Experimentation of the Institute of Clinical Medicine, China-Japan Friendship Hospital, Beijing. As shown in the pharmacokinetics profile of SN38&ICG/Gd&Yb-LDH (Fig. S20†), the blood circulation of SN38&ICG/Gd&Yb-LDH obeys the typical two compartment model, where the first phase (distribution phase with a rapid decline) gives a half-life of 0.621 ± 0.163 h and the second phase (elimination phase, the predominant process for nanoparticle clearance) gives a half-life of 9.65 ± 0.97 h. Moreover, the area under the curve (AUC) is determined to be 337 µg h mL^{-1} and the volume of distribution (V) is measured to be 1.94 mL $\pm$ 0.68 mL. The long blood circulation may delay the clearance of SN38&ICG/Gd&Yb-LDH and thus contribute to drug accumulation in tumours. The *in vivo* bio-distribution and accumulation process of SN38&ICG/

Gd&Yb-LDH in tumors were investigated by MR/CT/NIRF tri-mode imaging, which would offer both deep spatial resolution (MRI and CT) and high imaging sensitivity (NIRF). As shown in Fig. 5A, after the intravenous injection of SN38&ICG/Gd&Yb-LDH, the tumor site of Balb/c nude mouse displays a gradually enhanced MRI signal which reaches the strongest state after 12 h due to the enhanced permeability and retention (EPR) effects of SN38&ICG/Gd&Yb-LDH. Reconstructed three-dimensional (3D) CT imaging gives a similar result (Fig. 5B): the clearest tumor angiography is obtained at 12 h due to the preferential accumulation of SN38&ICG/Gd&Yb-LDH at the tumor site. Furthermore, the NIRF imaging performance was investigated *in vivo*. As shown in Fig. 5C, mice injected with SN38&ICG or SN38&ICG/Gd&Yb-LDH after 2 h exhibit NIRF signals throughout the whole body. Afterwards, a rather weak fluorescence signal at the tumor site is observed at 6 h for the former group, which fades quickly and disappears completely at 12–24 h. For the mice treated with SN38&ICG/Gd&Yb-LDH, however, a strong fluorescence signal at the tumor site is observed at 12 h and it remains constant even at 24 h. To further estimate the biodistributions of SN38&ICG/Gd&Yb-LDH, major organs and tumors were collected at different time points after intravenous injection of SN38&ICG/Gd&Yb-LDH. Fig. S21A† shows the *ex vivo* fluorescence images of various organs at 2 h, 6 h, 12 h, 24 h and 48 h, where the strongest fluorescence intensity of the tumor is found at 12 h. Furthermore, the time-dependent distribution of SN38&ICG/Gd&Yb-LDH in the tumor and various
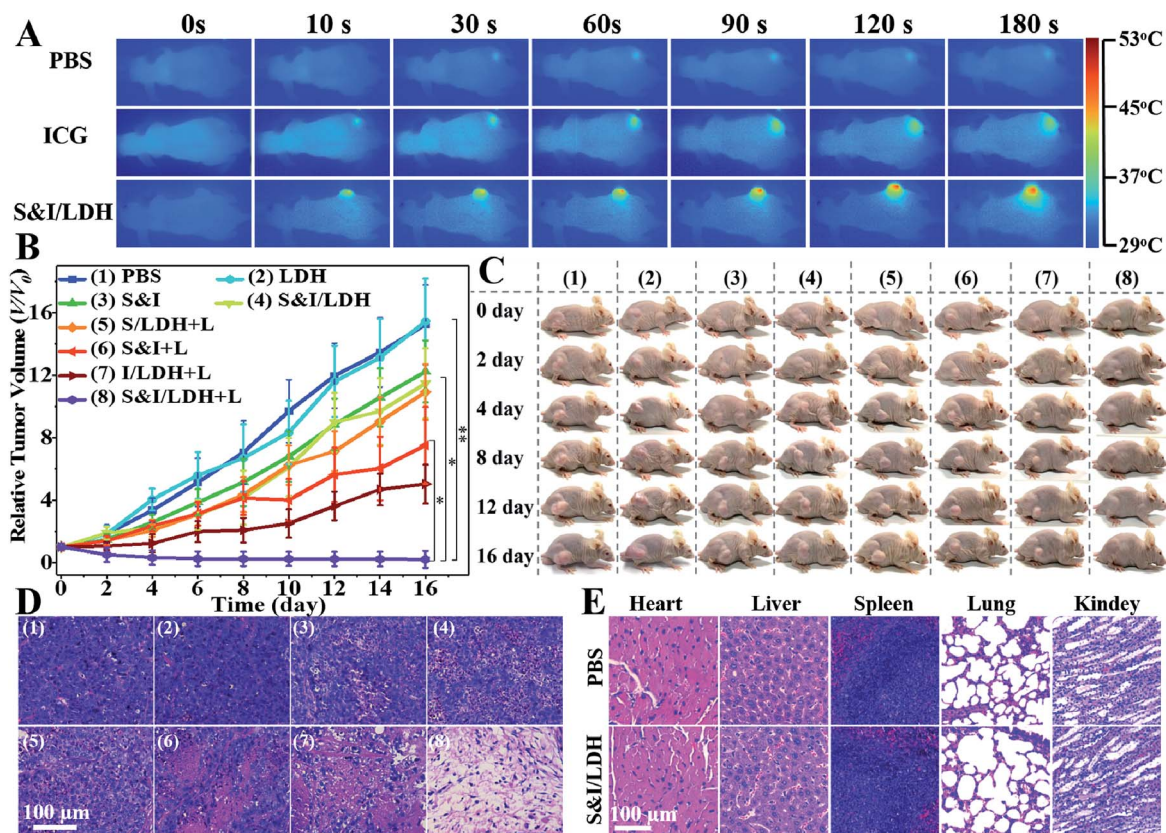
Fig. 6   (A) *In vivo* photothermal imaging of mice injected intravenously with PBS, ICG and SN38&ICG/Gd&Yb–LDH after 12 h with 3 min of irradiation. (B) Hela tumor growth curves with various drug treatments. (C) Digital photographs of mice with various drug treatments at different time points. (D) H&E stained tumor tissue slices from different groups of mice after 16 d of post-treatment. (E) Histological images of major organs collected on day 16 treated with PBS and SN38&ICG/Gd&Yb–LDH, respectively. *P* values in (B) were calculated by Tukey's post-test (***P < 0.001, **P < 0.01, or *P < 0.05).

organs was determined in Fig. S21B.† A high average fluorescence intensity is observed in the tumor, as well as in reticuloendothelial systems (RES) such as the liver, lung, and kidney, demonstrating an excellent permeability and retention (EPR) effect of SN38&ICG/Gd&Yb-LDH. The results above indicate the excellent passive targeted properties of SN38&ICG/Gd&Yb-LDH as well as a prolonged tumor retention time.

Based on the exciting results demonstrated above, the combined therapeutic ability of SN38&ICG/Gd&Yb-LDH was further investigated on mice bearing Hela tumors. Firstly, *in vivo* photothermal images were recorded after i.v. injection for 12 h (Fig. 6A). Within 3 min of NIR irradiation, the mice injected with ICG exhibit temperatures as high as 42 °C at the tumor site, while the mice injected with SN38&ICG/Gd&Yb-LDH show temperatures as high as 51 °C, which is beneficial to *in vivo* photothermal therapy. Subsequently, the mice were divided into eight groups: (1) PBS, (2) Gd&Yb-LDH, (3) SN38&ICG, (4) SN38&ICG/Gd&Yb-LDH, (5) SN38/Gd&Yb-LDH with irradiation, (6) SN38&ICG with irradiation, (7) ICG/Gd&Yb-LDH with irradiation, and (8) SN38&ICG/Gd&Yb-LDH with irradiation. The drug injection dose was 3 mg kg^{-1}, the irradiation (808 nm laser, 1.0 W cm^{-2}) was conducted for 3 min at 12 h post injection, and the tumor volume was monitored for 16 days (Fig. 6B). No obvious tumor inhibition is detected for the PBS or Gd&Yb-

LDH group, while SN38&ICG, SN38&ICG/Gd&Yb-LDH without irradiation and SN38/Gd&Yb-LDH with irradiation inhibit the tumor growth partially due to the chemotherapy of SN38. A remarkably enhanced therapeutic effect is found in the group of SN38&ICG and ICG/Gd&Yb-LDH with irradiation. In the case of SN38&ICG/Gd&Yb-LDH with irradiation, a complete tumor ablation is observed, demonstrating an excellent *in vivo* synergistic therapeutic effect with a rather low drug dose. Fig. 6C displays the digital photos of dynamic tumor growth and the corresponding excised tumors are shown in Fig. S22,† in accordance with the tumor volume curves. On staining with hematoxylin and eosin (H&E),[23] the tumor tissue collected from mice treated with SN38&ICG/Gd&Yb-LDH plus irradiation exhibits obvious necrosis while other groups only show partial necrosis or even retain their normal morphology (Fig. 6D). The weight of the mice increases slightly for every group during the treatment, indicating little side effect (Fig. S23†). In addition, *in vivo* toxicity of the SN38&ICG/Gd&Yb-LDH nanosheets was evaluated through i.v. injection of SN38&ICG/Gd&Yb-LDH into mice (200 μL, 10 mg kg^{-1}), and the results showed that all the blood biochemistry and liver and kidney function markers were maintained in the normal range compared with the PBS control group (Fig. S24†). Moreover, no further potential signs of toxicity were observed by comparing the SN38&ICG/Gd&Yb-LDH

group with the PBS group in the H&E analysis of major organs (heart, liver, spleen, lung, and kidney) (Fig. 6E), demonstrating a negligible toxicity of SN38&ICG/Gd&Yb-LDH.

Conclusions

In summary, we reported a facile "bottom-up" method for the preparation of monolayer Gd&Yb-LDH nanosheets, which serve as a promising drug carrier for imaging guided cancer therapy. The loading capacity of Gd&Yb-LDH nanosheets toward SN38 reaches 925%, far beyond that of previously reported drug carriers. In addition, by virtue of the co-doped rare earth elements (Gd^{3+} and Yb^{3+}) in the LDH host layer, SN38&ICG/Gd&Yb-LDH can provide real time feedback through tri-mode MR/CT/NIRF imaging, which facilitates visualization of drug bio-distribution for further effective treatment. For the *in vivo* tests with Hela tumor-bearing mice, the synergistic chemo/PTT/PDT therapy of SN38&ICG/Gd&Yb-LDH results in a complete ablation of tumors with minimum side effects. Therefore, the LDH monolayer nanosheets with precise control over the chemical composition and functionality provide a strategy to develop novel theranostic systems, holding potential for application in clinical cancer therapy.

Conflicts of interest

There are no conflicts to declare.

Acknowledgements

Notes and references

1 Y. Chen, C. Tan, H. Zhang and L. Wang, *Chem. Soc. Rev.*, 2015, **44**, 2681.

2 H. Wang, X. Yang, W. Shao, S. Chen, J. Xie, X. Zhang, J. Wang and Y. Xie, *J. Am. Chem. Soc.*, 2015, **137**, 11376.

3 L. Gao, Y. Wang, H. Li, Q. Li, N. Ta, L. Zhuang, Q. Fu and X. Bao, *Chem. Sci.*, 2017, **8**, 5728.

4 M. Acerce, D. Voiry and M. Chhowalla, *Nat. Nanotechnol.*, 2015, **10**, 313.

5 (a) J. D. Nunez, A. M. Benito, S. Rouziere, P. Launois, R. Arenal, P. M. Ajayan and W. K. Maser, *Chem. Sci.*, 2017, **8**, 4987; (b) B. R. Smith and S. S. Gambhir, *Chem. Rev.*, 2017, **117**, 901; (c) V. Nicolosi, M. Chhowalla, M. G. Kanatzidis, M. S. Strano and J. N. Coleman, *Science*, 2013, **340**, 1226419; (d) J. Xie, H. Zhang, S. Li, R. Wang, X. Sun, M. Zhou, J. Zhou, X. W. Lou and Y. Xie, *Adv. Mater.*, 2013, **25**, 5807; (e) P. Sun, R. Ma and T. Sasaki, *Chem. Sci.*, 2018, **9**, 33.

6 (a) D. Chimene, D. L. Alge and A. K. Gaharwar, *Adv. Mater.*, 2015, **27**, 7261; (b) M. Xiao, S. Wei, Y. Li, J. Jasensky,

J. Chen, C. Brooks and Z. Chen, *Chem. Sci.*, 2018, **9**, 1769; (c) H. Zhang, *ACS Nano*, 2015, **9**, 9451; (d) Y. Yang, Q. Zhao, W. Feng and F. Li, *Chem. Rev.*, 2013, **113**, 192; (e) G. Mikhaylov, U. Mikac, A. A. Magaeva, V. I. Itin, E. P. Naiden, I. Psakhye, L. Babes, T. Reinheckel, C. Peters, R. Zeiser, M. Bogyo, V. Turk, S. G. Psakhye, B. Turk and O. Vasiljeva, *Nat. Nanotechnol.*, 2011, **6**, 594.

7 (a) H. Wang, J. Zhang, X. Hang, X. Zhang, J. Xie, B. Pan and Y. Xie, *Angew. Chem., Int. Ed.*, 2015, **54**, 1195; (b) X. Ai, C. J. H. Ho, J. Aw, A. B. E. Attia, J. Mu, Y. Wang, X. Wang, Y. Wang, X. Liu, H. Chen, M. Gao, X. Chen, E. K. L. Yeow, G. Liu, M. Olivo and B. Xing, *Nat. Commun.*, 2016, **7**, 10432; (c) A. Chatterjee and K. Biswas, *Angew. Chem., Int. Ed.*, 2015, **54**, 5623; (d) J. H. Han, S. Lee and J. Cheon, *Chem. Soc. Rev.*, 2013, **42**, 2581; (e) J. Yu, J. Li, W. Zhang and H. Chang, *Chem. Sci.*, 2015, **6**, 6705.

8 (a) S. Jeong, D. Yoo, J.-t. Jang, M. Kim and J. Cheon, *J. Am. Chem. Soc.*, 2012, **134**, 18233; (b) W. Yang, L. Zhang, J. Xie, X. Zhang, Q. Liu, T. Yao, S. Wei, Q. Zhang and Y. Xie, *Angew. Chem., Int. Ed.*, 2016, **55**, 6716; (c) K. Ramasamy, H. Sims, W. H. Butler and A. Gupta, *J. Am. Chem. Soc.*, 2014, **136**, 1587; (d) A. H. M. Leung, S. D. Pike, A. J. Clancy, H. C. Yau, W. J. Lee, K. L. Orchard, M. S. P. Shaffer and C. K. Williams, *Chem. Sci.*, 2018, **9**, 2135.

9 (a) P. J. Sideris, U. G. Nielsen, Z. Gan and C. P. Grey, *Science*, 2008, **321**, 113; (b) S.-J. Choi, G. E. Choi, J.-M. Oh, Y.-J. Oh, M.-C. Park and J.-H. Choy, *J. Mater. Chem.*, 2010, **20**, 9463; (c) R. Tian, S. Zhang, M. Li, Y. Zhou, B. Lu, D. Yan, M. Wei, D. G. Evans and X. Duan, *Adv. Funct. Mater.*, 2015, **25**, 5006; (d) W. Liu, S. Xu, S. Guan, R. Liang, M. Wei, D. G. Evans and X. Duan, *Adv. Mater.*, 2018, **30**, 1704376.

10 (a) Q. Wang and D. O'Hare, *Chem. Rev.*, 2012, **112**, 4124; (b) R. Liang, R. Tian, L. Ma, L. Zhang, Y. Hu, J. Wang, M. Wei, D. Yan, D. G. Evans and X. Duan, *Adv. Funct. Mater.*, 2014, **24**, 3144; (c) Z. Gu, J. J. Atherton and Z. P. Xu, *Chem. Commun.*, 2015, **51**, 3024; (d) J.-M. Oh, M. Park, S.-T. Kim, J.-Y. Jung, Y.-G. Kang and J.-H. Choy, *J. Phys. Chem. Solids*, 2006, **67**, 1024.

11 (a) L. Li, W. Gu, J. Chen, W. Chen and Z. P. Xu, *Biomaterials*, 2014, **35**, 3331; (b) D.-H. Park, J.-E. Kim, J.-M. Oh, Y.-G. Shul and J.-H. Choy, *J. Am. Chem. Soc.*, 2010, **132**, 16735.

12 (a) R. Tian, D. Yan, C. Li, S. Xu, R. Liang, L. Guo, M. Wei, D. G. Evans and X. Duan, *Nanoscale*, 2016, **8**, 9815; (b) B. Li, Z. Gu, N. Kurniawan, W. Chen and Z. P. Xu, *Adv. Mater.*, 2017, **29**, 1700370.

13 (a) R. Gao and D. Yan, *Chem. Sci.*, 2017, **8**, 590; (b) Y. Zhao, B. Li, Q. Wang, W. Gao, C. J. Wang, M. Wei, D. G. Evans, X. Duan and D. O'Hare, *Chem. Sci.*, 2014, **5**, 951; (c) X. Mei, S. Xu, T. Hu, L. Peng, R. Gao, R. Liang, M. Wei, D. G. Evans and X. Duan, *Nano Res.*, 2018, **11**, 195; (d) Z. Li, M. Shao, H. An, Z. Wang, S. Xu, M. Wei, D. G. Evans and X. Duan, *Chem. Sci.*, 2015, **6**, 6624.

14 (a) H. Wang, H. Xie, J. Wu, X. Wei, L. Zhou, X. Xu and S. Zheng, *Angew. Chem., Int. Ed.*, 2014, **126**, 11716; (b) J. Wang, J. A. Kaplan, Y. L. Colson and M. W. Grinstaff, *Angew. Chem., Int. Ed.*, 2016, **55**, 2796; (c) Y. Shen, E. Jin, B. Zhang, C. J. Murphy, M. Sui, J. Zhao, J. Wang, J. Tang,

M. Fan, E. Van Kirk and W. J. Murdoch, *J. Am. Chem. Soc.*, 2010, **132**, 4259; (*d*) H. Wang, H. Xie, J. Wang, J. Wu, X. Ma, L. Li, X. Wei, Q. Ling, P. Song, L. Zhou, X. Xu and S. Zheng, *Adv. Funct. Mater.*, 2015, **25**, 4956; (*e*) K. Cai, J. Yen, Q. Yin, Y. Liu, Z. Song, S. Lezmi, Y. Zhang, X. Yang, W. G. Helferich and J. Cheng, *Biomater. Sci.*, 2015, **3**, 1061; (*f*) Y. Li, K. Xiao, J. Luo, J. Lee, S. Pan and K. S. Lam, *J. Controlled Release*, 2010, **144**, 314; (*g*) T. Liu, C. Wang, X. Gu, H. Gong, L. Cheng, X. Shi, L. Feng, B. Sun and Z. Liu, *Adv. Mater.*, 2014, **26**, 3433; (*h*) H. Wang, J. Chen, C. Xu, L. Shi, M. Tayier, J. Zhou, J. Zhang, J. Wu, Z. Ye, T. Fang and W. Han, *Theranostics*, 2017, **7**, 3638; (*i*) H. Wang, Z. Lu, L. Wang, T. Guo, J. Wu, J. Wan, L. Zhou, H. Li, Z. Li, D. Jiang, P. Song, H. Xie, L. Zhou, X. Xu and S. Zheng, *Cancer Res.*, 2017, **77**, 6963; (*j*) Z. Liu, J. T. Robinson, X. Sun and H. Dai, *J. Am. Chem. Soc.*, 2008, **130**, 10876.

15 (*a*) F. Song and X. Hu, *Nat. Commun.*, 2014, **5**, 4477; (*b*) D. Yan, J. Lu, J. Ma, M. Wei, D. G. Evans and X. Duan, *Angew. Chem., Int. Ed.*, 2011, **123**, 746.

16 Y. Li, X. Hu, D. Ding, Y. Zou, Y. Xu, X. Wang, Y. Zhang, L. Chen, Z. Chen and W. Tan, *Nat. Commun.*, 2017, **8**, 15653.

17 D. L. Longo, P. Z. Sun, L. Consolino, F. C. Michelotti, F. Uggeri and S. Aime, *J. Am. Chem. Soc.*, 2014, **136**, 14333.

18 P. Huang, X. Qian, Y. Chen, L. Yu, H. Lin, L. Wang, Y. Zhu and J. Shi, *J. Am. Chem. Soc.*, 2017, **139**, 1275.

19 M. Grossi, M. Morgunova, S. Cheung, D. Scholz, E. Conroy, M. Terrile, A. Panarella, J. C. Simpson, W. M. Gallagher and D. F. O'Shea, *Nat. Commun.*, 2016, **7**, 10855.

20 F. Liu, X. He, H. Chen, J. Zhang, H. Zhang and Z. Wang, *Nat. Commun.*, 2015, **6**, 8003.

21 W. Malin, D. Cecilia, S. Takashi, M. Jelena, B. Ninib, F. M. Ole, L. Rolf, K. Per, Z. G. Peter and J. I. John, *Int. J. Cancer*, 2013, **132**, 1516.

22 J. Shi, L. Wang, J. Gao, Y. Liu, J. Zhang, R. Ma, R. Liu and Z. Zhang, *Biomaterials*, 2014, **35**, 5771.

23 G. Yang, L. Xu, Y. Chao, J. Xu, X. Sun, Y. Wu, R. Peng and Z. Liu, *Nat. Commun.*, 2017, **8**, 902.